

**Lithological control on the kinematic pattern and the location of slip surfaces in a large clayey landslide (Trièves, French Alps)**

Journal:	<i>Earth Surface Processes and Landforms</i>
Manuscript ID:	ESP-11-0402
Wiley - Manuscript type:	Paper
Date Submitted by the Author:	23-Dec-2011
Complete List of Authors:	Bièvre, Grégory; Centre d'Etudes Techniques de Lyon, Laboratoire de Lyon; Université de Grenoble 1, ISTerre Jongmans, Denis; Université Grenoble 1, ISTerre Goutaland, David; Centre d'Etudes Techniques de Lyon, Laboratoire d'Autun Zumbo, Vilma; Inexia, Ingénierie
Keywords:	landslide, clay, drainage, kinematics, geophysics

SCHOLARONE™  
Manuscripts

Review

Lithological control on the kinematic pattern and the location of  
slip surfaces in a large clayey landslide (Trièves, French Alps)

Grégory Bièvre<sup>a,b,1</sup>, Denis Jongmans<sup>b</sup>, David Goutaland<sup>c</sup> and Vilma Zumbo<sup>c,d</sup>

a Centre d'Études Techniques de Lyon, Laboratoire de Lyon, 25 avenue François  
Mitterrand, 69674 Bron cedex, France.

b ISTERre, Université de Grenoble 1, CNRS, BP 53, 38041 Grenoble Cedex 9, France.

c Centre d'Études Techniques de Lyon, Laboratoire d'Autun, BP 141, 71404 Autun  
cedex, France.

d Inexia Ingénierie, 1 place aux étoiles, 93212 Saint-Denis-La-Plaine cedex, France.

Abstract

Although it has been studied for more than 30 years, the large clayey Avignonet  
landslide (western French Alps) exhibits a heterogeneous kinematic pattern which is  
still poorly understood. Conducting electrical resistivity tomography profiles over  
the whole landslide has allowed the presence of a superficial coarser layer to be  
detected in its upper north-western part. The extension of this more permeable  
layer matches the zone exhibiting low slide velocities values (lower than 2 cm/yr),  
suggesting a lithological and hydrogeological control on the landslide activity. The  
presence of this coarser layer was not detected before, because investigation ef-  
forts concentrated on the southern inhabited areas where displacement rates are

<sup>1</sup>corresponding author ([gbievre@ujf-grenoble.fr](mailto:gbievre@ujf-grenoble.fr); Tel.: +33 (0)6 64 49 31 27)

the highest (10 cm/yr to 50 cm/yr) and the slope is only composed of laminated clays. Combined interpretation of seismic reflected waves and geological data has also evidenced the presence of a 10 m thick sandy alluvial layer interbedded in the clayey sequence. Comparison between reflectors and slip surfaces detected in boreholes suggests a significant role of this coarse layer on the location of the deepest slip surface at about 40 m. This study highlights the control of both vertical and horizontal lithological variations on the Avignonet landslide process and the necessity of combining various investigation techniques for understanding the complexity of large landslide mechanism.

**keywords:** landslide, clay, drainage, kinematics, geophysics

1  
2  
3  
4  
5  
6  
7  
8  
9  
10  
11  
12  
13  
14  
15  
16  
17  
18  
19  
20  
21  
22  
23  
24  
25  
26  
27  
28  
29  
30  
31  
32  
33  
34  
35  
36  
37  
38  
39  
40  
41  
42  
43  
44  
45  
46  
47  
48  
49  
50  
51  
52  
53  
54  
55  
56  
57  
58  
59  
60

# 1 Introduction

Slow-moving landslides frequently affect gentle slopes made of clayey formations, with volumes which can range from a few m<sup>3</sup> to several tens of millions of m<sup>3</sup> (Picarelli, 2000; Eilertsen et al., 2008). These landslides frequently exhibit sudden acceleration phases and flows, which can be triggered by changes in the stress field (pore pressure increase, loading, erosion) or modifications in the soil characteristics (weathering, leaching or pollutant infiltration; Picarelli et al., 2004; Van Asch et al., 2006; Eilertsen et al., 2008). Understanding landslide behaviour first requires the characterization of the ground surface kinematics, which can be achieved through punctual measurements, like GPS or optical devices (Stiros et al., 2004; Corsini et al., 2005), or more recently through dense displacement maps provided by digital photogrammetry (Baldi et al., 2008), laser scanning (Corsini et al., 2007; Teza et al., 2008) or Synthetic Aperture Radar interferometry (InSAR; Rott et al., 1999; Squarzoni et al., 2003; Strozzi et al., 2005). Continuous punctual measurements provide excellent temporal resolution with low spatial resolution. On the contrary, InSAR and Laser scanning, whose sensors can be attached to aerial or ground platforms, are limited in terms of temporal resolution.

Displacement measurements on clayey landslides usually display a spatially heterogeneous field, with zones of higher activity which can evolve with time (Squarzoni et al., 2003; Corsini et al., 2005; François et al., 2007; Baldi et al., 2008; Travelletti et al., 2011). While temporal variations are usually interpreted as resulting from pore pressure fluctuations, the spatial variability in the surface displacement has been related to various factors, including geological heterogeneity, the presence of discontinuities, the existence of several imbricate slip surfaces or the landslide mechanism itself. At the Tessina landslide in northern Italy, which affects quickly-evolving Tertiary Flysch deposits, Petley et al.



(2005) performed a detailed study of surface displacement series. They evidenced four distinct movement patterns, from slow movements at the crown (about 1 mm/day) to episodic and rapid movements (1 m/day) in the accumulation zone in which mudflows can occur. The pattern evolution is associated with the disintegration of blocks to loose material when moving downward. Even if this model could fit numerous observations on landslides in clayey soft rocks, additional complexity in the surface and underground kinematic pattern can arise from geological heterogeneity (Corsini et al., 2005; Squarzoni et al., 2003; Travelletti and Malet, 2011). A first reported example is the Corvara landslide (Dolomites, NE Italy) affecting Triassic weak clayey rock masses, whose 3D structure was thoroughly investigated and which was monitored during one year using differential GPS and borehole measurements (Corsini et al., 2005). Maximum horizontal sliding velocities were recorded in the track zone but also in the uppermost part of the accumulation zone. Several slip surfaces were found by borehole devices at depth ranging from 10 m to 48 m, and their overlapping and differential activity could explain local increase in sliding velocities. Moreover, some of them were related to coarser horizons which could act as confined aquifers (Corsini et al., 2005). This vertical geological heterogeneity was thought to have played a significant role in the landslide mechanism and evolution. This effect was also evidenced in submarine translational slides, in which Harders et al. (2010) found that a few centimeters thick intercalated volcanic tephra layer marks the detachment surface, as well as in a Flysch formation in the Betic cordillera (Southern Spain), where Azañón et al. (2010) showed that slip surfaces developed on smectite-rich clay layers. Finally, studying the crown of the la Valette landslide (France), Travelletti and Malet (2011) evidenced a strong lateral influence of tectonic discontinuities on the kinematic pattern and the retrogression mechanism.

The aim of this study is to highlight the control of lithology on the location of slip surfaces and on the surface displacement rate field at the large clayey landslide of Avignonet (France). Although this landslide has been extensively studied, this influence has not been reported before, owing to a bias in the investigation that concentrated in inhabited areas. The detection of coarser layers at the surface and at depth was made possible by the application of geophysical methods and was validated by geological observations and surface permeability measurements. Electrical imaging of the superficial coarser layer allowed a new interpretation of the displacement field. As already pointed out before, this case history illustrates the necessity of combining investigation and monitoring techniques for understanding the complexity of large landslide mechanism behaviour.

## 2 Study site

### 2.1 Geological and geotechnical background

The Trièves area, located 40 km south of the city of Grenoble, is a 300 km<sup>2</sup> plateau made of Quaternary glacio-lacustrine deposits and surrounded by carbonate and crystalline mountain ranges. These sediments, which were deposited during the Last Glacial Maximum (LGM) in a glacially-dammed lake, show a rhythmic alternation of clayey and silty laminae (millimetre to decimetre thick; [Giraud et al., 1991](#)). They overlay a local Quaternary compact and locally cemented alluvial formation (made of a succession of sand, gravel and pebble layers) and a Mesozoic bedrock consisting of Jurassic marly limestones (see the geological map and cross-section in Figures 1a and 1b, respectively). The paleotopography of the former Trièves Lake is irregularly shaped, inducing a dramatic variation in clay thickness, from 0 to nearly 300 m (Fig. 1; [Bièvre et al., 2011b](#)). The laminated

clays are locally capped by a few m to a few tens of m thick till layer, evolving into a morainic colluvium of a few m thick along the slopes (Figure 1b). Since the retreat of the glacier 14 ky ago (Brocard et al., 2003), the Drac river has cut into the soft (moraines and laminated clays) and compact (alluvial layers and marly limestones) layers and has initiated numerous landslides in the clayey formations. Presently, 15 % of the Trièves area is estimated to be sliding (Requillard and Moulin, 2004).

The large translational landslide of Avignonet is located east of the village of Sinard, along the man-made Monteynard Lake (Figure 1a). This landslide, whose first signs of instability were noticed between 1976 and 1981 (Lorier and Desvarreux, 2004), affects a surface of about  $1.6 \times 10^6 \text{ m}^2$ . LiDAR data (airborne light detection and ranging) was collected in November 2006 using a laser scanner mounted on a helicopter (Bièvre et al., 2011b). Since 1995, the landslide activity has been monitored twice a year from GPS measurements performed at 25 locations (Jongmans et al., 2009). Two permanent GPS stations points were installed in 2007 and 1 additional point was monitored during one year in 2008. Interpretation of mean sliding velocities measured at these 28 stations has evidenced an eastward motion and an increase in velocity, from 0-2 cm/yr at the top to 3-4 cm/yr in the lower part of the landslide. An active zone exhibiting velocities higher than 10 cm/yr (and up to 50 cm/yr) was detected in the eastern and southern part of the landslide (Figure 2). This activity was confirmed from the morphological study of the LiDAR-induced digital elevation model. Most of the geotechnical investigation was carried out in the southern most active part of the slide, where housing development took place in the late seventies. Five boreholes were performed (T0 to T3 in 1981 and T4 in 2009) in this area to locate and characterize the rupture surfaces. The four first ones were equipped with inclinometers while the fifth one was cored, allowing the lithological

1  
2  
3  
4  
5  
6  
7  
8  
9  
10  
11  
12  
13  
14  
15  
16  
17  
18  
19  
20  
21  
22  
23  
24  
25  
26  
27  
28  
29  
30  
31  
32  
33  
34  
35  
36  
37  
38  
39  
40  
41  
42  
43  
44  
45  
46  
47  
48  
49  
50  
51  
52  
53  
54  
55  
56  
57  
58  
59  
60

124 and geotechnical characteristics to be studied. Borehole results (Jongmans et al., 2009;  
125 Bièvre et al., 2011a) are summarized in Table 1. They evidenced three main slip surfaces:  
126 one at about 5 m at the bottom of the morainic colluvium layer, and two inside the clay  
127 layer, between 10 and 20 m and between 40 and 50 m deep, respectively. Three boreholes  
128 (T0 to T2) encountered alluvial layers (silts, sands and pebbles) at their bottom, at an  
129 elevation between 620 m and 636 m asl. Water level is superficial (a few m depth) with  
130 seasonal variations of about 1 to 2 m.

## 131 2.2 Geophysical setting

132 Previous geophysical investigation of the landslide (Jongmans et al., 2009; Renalier et al.,  
133 2010a,b; Bièvre et al., 2011a,b) was also focused in the southern part of the Avignonet  
134 landslide (south of the line joining T0 and T2; Figure 2), which encompasses the more ac-  
135 tive zones and populated areas. Geophysical survey included seismic noise measurements,  
136 electrical resistivity tomography, P and S-wave seismic refraction tomography and surface  
137 wave inversion. Electrical and P-wave velocity ( $V_p$ ) images showed that, below the few m  
138 thick colluvium layer, the ground down to 40 m depth is mainly made of saturated clay,  
139 with slight variations in  $V_p$  and electrical resistivity. On the contrary, S-wave velocity  
140 ( $V_s$ ) exhibits significant lateral and vertical variations, in agreement with slip surfaces  
141 and morphological features.  $V_s$  values measured at shallow depth (5-10 m) were found  
142 to be inversely correlated with displacement rates measured by GPS (Jongmans et al.,  
143 2009), with a division by at least a factor of 2 between the zones unaffected and strongly  
144 deformed by the landslide. In a further study, the cross-correlation technique was suc-  
145 cessfully applied to seismic noise records for 3D  $V_s$  imaging of the Avignonet landslide  
146 (Renalier et al., 2010b) to a depth of 50 m. Combining some of these results with seismic

1  
2  
3 147 noise measurements (H/V method), [Bièvre et al. \(2011b\)](#) derived a paleotopography map of  
4  
5 148 the bedrock below the landslide. Finally, at the decameter scale, geophysical techniques  
6  
7 149 (time-lapse electrical tomography and surface wave studies) underlined the role of the  
8  
9 150 fissures affecting the surface in the southern part of the landslide as preferential paths for  
10  
11 151 water infiltration ([Bièvre et al., 2011a](#)).  
12  
13  
14  
15

### 16 2.3 New investigation campaign

17  
18  
19 153 The geotechnical and geophysical data acquired so far, predominantly in the southern part  
20  
21 154 of the landslide, are however unable to explain two major features of the landslide, *i.e.*, 1)  
22  
23 155 the spatial variation observed in the displacement rate field and 2) the depth of the slip  
24  
25 156 surfaces into the clay. The observation of reflected waves during refraction experiments  
26  
27 157 and local geological observations however suggested that the laminated clay layer, usually  
28  
29 158 considered as homogeneous at the meter to the decametre scale ([Giraud et al., 1991](#)) could  
30  
31 159 exhibit some significant lithological vertical and lateral variations over the landslide. In  
32  
33 160 order to verify this hypothesis, five investigation surveys were performed: 1) a geological  
34  
35 161 survey of the outcrops at the vicinity of the landslide, 2) the processing of reflected waves  
36  
37 162 appearing on the records of three 470 m long seismic refraction profiles, 3) an electrical  
38  
39 163 campaign covering the whole landslide area, 4) borehole televiwer logging in two new  
40  
41 164 20 m long boreholes, and 5) five hydrological infiltration tests to enhance the hydraulic  
42  
43 165 properties of the ground.  
44  
45  
46  
47  
48  
49

## 50 3 Methods

51  
52  
53 167 The reflected events detected in the records of three existing 470 m-long seismic refraction  
54  
55 168 profiles (SR1 to SR3; location in Figure 2) were processed using the Reflexw package  
56  
57  
58  
59  
60

(Sandmeier, 2010). Acquisition was made with 48, 4.5 Hz, vertical geophones linearly spread each 10 m. Seven to ten explosive sources were fired along each profile and 2 to 3 offset shots were made, depending on the accessibility. The traces recorded by a single shot were grouped together (common shot point technique) and a velocity analysis was carried out independently for each shot, applying the Dix formula (Dix, 1955). Ten ERT (Electrical Resistivity Tomography) profiles, labelled E1 to E10, were conducted over the landslide (Figure 2). ERT profiles were acquired using the Wenner configuration with the acquisition parameters given in Table 2. The high water content and clayey nature of the ground allowed a very good electrical coupling between the electrodes and the ground, generating a high signal to noise ratio for measurements. Apparent resistivity data were processed using a median filter to remove strong outliers and were inverted according to the L1-norm with the algorithm developed by Loke and Barker (1996). Acceptable absolute errors (lower than 5 %) were reached for a maximum of 3 iterations (Table 2). The reliability of inversions was furthermore assessed with the DOI (Depth of Investigation) index proposed by Oldenburg and Li (1999). Results (not presented here) confirmed the robustness of the inversion process. BHTV logging (BoreHole TeleViewer; Serra, 2008) with 1.2 MHz acoustic waves was conducted in two 20 m deep boreholes labelled T4a and T4b and located 8 m west and 9 m east from T4, respectively (Figure 2; these two boreholes are not drawn in the figure). The boreholes, spaced by 8 m along a South-North direction, were equipped with a casing, which in T4b was furthermore sealed to the ground. BHTV measurements were made in August 2009 (16 months after the drilling operations) to image the casing deformation and to locate slip surfaces in the first 20 m.

Finally, hydrological infiltration tests were carried over the landslide, at 5 sites ex-

hibiting both contrasted slide velocity values and geophysical properties. The technique employed, known as Beerkan infiltration method, was pioneered by Braud et al. (2005) and has been successively improved by Lassabatère et al. (2006) and Yilmaz et al. (2010). Experiments consist in measuring the time required for the infiltration of successive known volumes of water (in this work, typically 100 to 200 ml) through a single annular ring at null pressure head. The soil is sampled before and after the infiltration, in order to determine the particle size distribution, the dry bulk density and the volumetric water content. Unsaturated hydraulic properties are estimated through the analysis of the particle size distribution and the cumulative infiltration, using the BEST algorithm (Lassabatère et al., 2006). Infiltration experiments are conducted at a few tens of cm depth (generally between 20 and 30 cm) to avoid root zone. For short times, water infiltrates through the unsaturated soil with a transient regime whereas, for longer times, infiltration takes place within a saturated soil with a steady-state regime. Saturated hydraulic conductivity ( $K_s$ ) is estimated hypothesizing uniform soil, while steady-state infiltration rate (SIR) is derived from the slope of the cumulated infiltration curve for longer times.

## 4 Geological survey

Clay outcrops around the Avignonet landslide have been systematically visited. Figure 3a is a panorama taken from the eastern shore of the lake, showing the succession of geological layers. The underlying bedrock and compact alluvial layers appear as cliffs or high slopes, while the slope angle decreases to less than  $15^\circ$  in the overlying thick clay layer. The clay bottom is then expressed by a break in the slope, which is located at an elevation of 610 masl (above sea level) at this site. A bare gullied area undergoing intense erosion is visible in the clay layer below the Avignonet landslide. Geological survey in this zone

has evidenced the presence of a soft sandy to gravelly layer of about 10 m thick, which is interbedded in the clay, 15 m over the clay layer bottom (Figure 3b). This layer is made of dm to m thick near-horizontal beds of sand, gravels and pebbles (Figure 3c) and is non-conformably overlaid by slightly tilted laminated clays which dip to the South. The layer, whose top is located at an elevation of 635-640 masl, pinches to the south. This coarse geological formation is interpreted as a glaciofluvial deposit, whose source was probably located to the N-NW, close to the Isère glacier front. The presence of this layer indicates that clay deposits are not regular and could exhibit vertical and lateral facies variations below the landslide, as it was already described at other sites of the Trièves plateau (Monjuvent, 1973).

## 5 Geophysical results

### 5.1 P-wave seismic reflection analysis

Reflected waves were observed on the records of the three 470 m-long profiles S1 to S3 (Figure 2). Figure 4a presents the raw seismograms recorded for a central shot at 240 m along profile S1, which show refracted (Rf), reflected (Re) and Rayleigh surface waves (SW). Band-pass filtering between 100 and 600 Hz and automatic gain correction between 50 and 150 ms were applied to enhance reflections. After processing, three main reflections (labelled R1 to R3) are clearly visible at zero-offset times of 0.074 s, 0.165 s and 0.256 s, respectively (Figure 4b). Two other minor reflectors are barely distinguishable and will not be considered. Velocity analysis considering the 3 main reflections yields the velocity-depth profile shown in Figure 4c. Seismic velocities rise from about 1800 m/s at the surface to 2300 m/s at 260 m, resulting from the general increase of compactness with



depth. The three reflectors were found at 45 m, 145 m and 255 m depth, respectively. In the considered frequency range, the vertical resolution is assessed between 5 m (a quarter of the wavelength) and 10 m (half the wavelength; Telford et al., 1990). Owing to the limited number of sources, signals were gathered by shot (common shot point technique) and a velocity analysis similar to the one showed in Figure 4c was made for each shot along the three profiles. The position of the three reflectors (labelled R1 to R3) below each shot were projected on a mean West-East orientated geological cross-section (Figure 4d) derived from previous works (Bièvre et al., 2011b).

Considering the depth uncertainty, the three reflectors appear to be laterally continuous. The deepest near-horizontal reflector, located at an elevation of 520-540 m, fits the base of the clay layer, which overlies the seismic substratum made of compact, locally cemented alluvial layers and Mesozoic bedrock. The substratum topography appears to be locally irregular, as it has been previously shown by Bièvre et al. (2011b) from seismic noise measurements. The shallowest and strongest reflector R1 is near-parallel to the slope at a depth ranging between 40 m and 50 m. To the east of the cross-section, this reflector approximately corresponds to the deep slip surface evidenced in boreholes T0, T1 and T4 (Figure 4d). To the west, this reflector noticeably extends beyond the Avignonet landslide head scarp below the Sinard plateau. Finally, the near-horizontal intermediate reflector R2, located within the clay layer at an elevation of 620-640 m asl, is unexpected. Geological logs of boreholes T0 to T3 at that depth have encountered a few m of alluvial deposits made of a mixture of silts, sands and pebbles. The elevation of this coarse layer top fits the outcropping 10 m thick soft alluvial layer observed along the slope (see Figures 3 and 4f). The observed reflected waves R2 could then result from the presence of this continuous interbedded alluvial layer, whose thickness (about 10 m)

is too close to the seismic resolution for distinguishing the reflections at the layer top and bottom. At the extreme east of the cross-section, between T1 and T3, the rising of the bedrock and the convergence of the two shallow reflectors do not allow the three reflected events to be discriminated.

An interpretative cross-section was built from the analysis of P-wave reflections and geological and geotechnical data (Figure 5a). In the eastern part, reflector R1 corresponds to the deep slip surface detected in the boreholes, at a depth ranging between 40 and 50 m. To the West, it extends below the Sinard plateau at a similar depth, further westward than the present-day landslide head-scarp (Figure 5a). Considering the relatively high seismic velocity contrast evidenced across this reflector (Figure 4c), this result indicates that the superficial 40 m thick layer is deconsolidated and suggests an undergoing westward regression of the landslide. An alternative explanation is the possible role of the permafrost, which could have reached a thickness of a few tens of m during the Holocene (Matsuoka et al., 1998) and could have regionally degraded the upper part of the ground. To the east of the cross-section, the reflectors R1 and R2 converge, suggesting that the deep slip surface is partly controlled by the interbedded alluvial layer SA (see interpretation 1 in Figure 5b). This is corroborated by the inclinometer data in T2, which evidenced a slip surface 2.5 m over the alluvial layer top (Table 1). However, this slip surface could be a shallower one and the soft alluvial layer SA could be cut by the deep rupture surface (see intrerpretation 2 in Figure 5b). Finally, reflector R3 allows identifying the interface between the soft layers and the underlying compact alluvial layer and bedrock.

## 5.2 BoreHole TeleViewer (BHTV)

Acoustic imaging was carried out in two cased boreholes (T4a and T4b) to localize slip surfaces in the range 0-20 m, which cannot be resolved by the P-wave reflection method. Figure 6 shows the 3D images of the casing interior, as well as some horizontal slices (BHTV cross-sections) obtained at given depths in the two boreholes. Slices are positioned with respect to the North and to the central vertical axis (grey cross). Borehole T4a is affected by two shear deformations (Figure 6a): a slight one at 5 m depth which out-centred the casing south-eastward, and a strong one at 10.3 m, which probably broke the casing, as shown by the complex reflection pattern. A second strong deformation, located 1 m below (at 11.3 m), is probably associated to the previous one. Similarly, two strong deformations are observed on acoustic images in T4b, at depths of 2.5 and 10 m, with an acoustic image indicating that the casing is probably broken (Figure 6b). The sealing of the casing in T4b enables to detect slighter deformations at 5 m and 1 m (Figures 6c and 6d, respectively). BHTV measurements have then evidenced three main shear deformation levels at about 1-2.5 m, 5 m and 10-11 m. Slip Surfaces at 5 m and 10-11 m were previously identified by inclinometers and seismic prospecting (Figure 6a; Jongmans et al., 2009; Renalier et al., 2010a). On the contrary, the very shallow slip surface between 1 and 2.5 m was not detected by geophysical measurements, probably because of the relatively large geophone spacing (5 m).

## 5.3 Electrical Resistivity Tomography (ERT)

The 10 acquired electrical images (see Figure 2 for location) are shown with a common resistivity scale in Figure 7. Resistivity values range from 20 to 125  $\Omega$ .m. As measurements were carried out at varying periods of the year, the few m thick unsaturated shallow

layer, which can exhibit resistivity variations depending on meteorological conditions, is not described. Looking at the resistivity images, a clear contrast appears between the southern and northern parts of the slides.

In the northern part (profiles E1 to E4; Figure 7), resistivities are around  $100\ \Omega\cdot\text{m}$  for an elevation higher than about 690-700 m asl. Below this elevation, resistivities decrease rapidly to less than  $50\ \Omega\cdot\text{m}$ , a value characterizing fine-grained material. To the south, the more resistive layer progressively vanishes (E5 and E6; Figures 7d and 7e) and the ground evolves to a totally conductive formation (E8 and E9) with resistivity below  $30\ \Omega\cdot\text{m}$  (and down to  $20\ \Omega\cdot\text{m}$ ). These low values correspond to the saturated laminated clays, as evidenced by previous geophysical and geological studies in this area (Jongmans et al., 2009). However, the presence of thick (locally more than 30 m) upper resistive layer in the northern part of the slide was unexpected, as it is not mapped on the geological map (Figure 1a). Its origin will be discussed further. The lateral resistivity variations (from 20 to  $50\ \Omega\cdot\text{m}$ ) observed in the laminated clay layer probably result from the presence of a varying percentage of rock blocks and gravel in this formation, as it was found in borehole T4 (Bièvre et al., 2011a). Going downhill, resistivities also decrease along the slope from around  $100\ \Omega\cdot\text{m}$  above 700 m asl to less than  $30\ \Omega\cdot\text{m}$  at the bottom of the slide (see profiles E4, E5, E7 and E10; Figure 7). Below 530-540 m asl (profile E10), resistivities dramatically increase to  $700\ \Omega\cdot\text{m}$  in the Mesozoic bedrock (MB) that outcrop nearby (Figures 1 and 2).

In summary, ERT results show significant N-S and downhill resistivity variations within the Avignonet landslide. A resistive ( $100\ \Omega\cdot\text{m}$ ) and probably coarser formation is located above 700 m asl in the north-western part of the slide. This layer, whose thickness varies between 0 and 30 m over the site, pinches to the South and downslope, laterally

passing to laminated clays (resistivity ranging between 20 and 50  $\Omega$ .m).

## 6 Hydrogeological tests

The observed differences in resistivity, which is interpreted as resulting from a variation in grain-size distribution, should generate a permeability contrast between the two formations. Five hydrological infiltration tests (labelled i1 to i5) were carried out in different zones of the landslide (see location in Figure 8). Test i1 was positioned at an elevation of 720 m asl along profile E4 (Figure 7c), where resistive levels outcrop. This elevation also corresponds to the altitude of two water catchments and of a resurgence (Figure 8). Test i2 is located downslope along the same profile, in the clay layer, while i3 was performed more to the south, over the vanishing resistive layer. The last two tests (i4 and i5) were conducted in the south of the Avignonet landslide, at the vicinity of the active zone where low resistivity levels are found ( $< 30 \Omega$ .m; Figures 7g and 8).

Laboratory tests were performed on soil samples and results are presented in Table 3. Cumulative infiltration curves as a function of time are given in Figure 9. For test i1, a fast infiltration rate and a high hydraulic conductivity  $K_s$  ( $2.1 \times 10^{-5}$  m/s) were measured, consistently with the high porosity and the grain size distribution that indicates that more than 50 % of the soil is made of sand and gravel (Table 3). On the contrary, infiltration test i2, carried out downhill in the electrically conductive zone, yields a very low  $K_s$  value ( $8.1 \times 10^{-7}$  m/s) in a soil mainly composed of clay and silts (65 %). Southwards, test i3 found a  $K_s$  value ( $2.0 \times 10^{-6}$  m/s) lower than in test i1 for a finer material (almost 66 % of clays and silts). These results are in agreement with the southward and downslope vanishing of the resistive layer. For tests i4 and i5, infiltration curves (Figure 9) show a double permeability, indicating a non-homogenous soil and preventing from determining

the hydraulic conductivity. Infiltration rates SIR values of  $4 \times 10^{-5}$  m/s and  $4 \times 10^{-6}$  m/s,  $4 \times 10^{-5}$  m/s and  $1 \times 10^{-5}$  m/s were computed for short and long times, for i4 and i5, respectively (Figure 9). These values are relatively high, particularly in the case of i5, for which nearly 92% of the soil is made of silts and clays (Table 3). This apparent discrepancy probably results from the presence of numerous superficial fissures in this active zone (Bièvre et al., 2011a), which have increased the infiltration rates. Short-term higher values of SIR then probably correspond to the fissure permeability, while the lower ones reflect water infiltration through both the fissures and the soil matrix.

## 7 Discussion and conclusions

A 3D synthetic geological and geotechnical cross-section (Figure 10) has been built from the data interpretation, assuming the northward spatial continuity of the alluvial layer SA. This interpretation shows the relation between the slide velocity values, the slip surfaces and the spatial geological variations.

Combination of various geophysical data (reflection analysis, borehole logging) and geological observations (outcrops and borehole) suggests that the deep slip surface between 40 and 50 m is probably controlled by a vertical geological heterogeneity in the laminated clays (Figure 10). Re-interpretation of seismic profiles and borehole logs, associated with geological observation, consistently shows the existence of a 10 m thick sandy alluvial layer (SA) interbedded in the laminated clay, whose westward extension into the slope at greater depth has been identified with reflected waves. Another shallower reflector was found to match the deepest slip surface of the landslide (at about 40 m depth). The eastward convergence of these two reflectors, along with the depths of slip surfaces and of the sand layer top, supports the control of this layer on the deep rupture process (Line

1  
2  
3 1, Figure 10). However, the crossing of the sand layer by this deep slip surface (Line 2  
4  
5  
6 376 in Figure 10) cannot be excluded with the data at hand. In both interpretations, the  
7  
8 377 presence of the soft alluvial layer or of the ridge of hard layers (Figure 10) prevents the  
9  
10 378 slide from deep and rapid evolution as observed for the Harmalière landslide to the South  
11  
12 379 (Bièvre et al., 2011b). Finally, several shallower slip surfaces were evidenced at 10-15 m,  
13  
14 380 5 m and 1-2.5 m, in agreement with existing inclinometer data. The presence of such  
15  
16 381 multiple slip surfaces illustrates the complexity of deformation processes in clayey slopes,  
17  
18 382 as it has been previously shown in other large clay-rich landslides (e.g. Corsini et al.,  
19  
20 383 2005; Travelletti and Malet, 2011). In agreement with Bromhead and Ibsen (2004) and  
21  
22 384 Coe et al. (2009), these results also show that the subsurface geometry and geology is a  
23  
24 385 key-parameter to better define the geometry and pattern of slip surfaces at depth. The  
25  
26 386 northward extension of the interbedded alluvial layer, as well as the probable existence  
27  
28 387 of the multiple surfaces below the whole landslide, has however still to be proven.  
29  
30 388

31  
32 The electrical survey has evidenced the presence of a superficial resistive layer (around  
33  
34 389 100  $\Omega$ .m) in the north-western part of the landslide, which overlies the conductive lami-  
35  
36 390 nated clays (20-50  $\Omega$ .m) at an elevation around 700 m asl. Its thickness varies from 0 m to  
37  
38 391 more than 30 m at the North-western limit of the landslide. Unfortunately, no borehole  
39  
40 392 was performed in this less active part to characterize this formation. Resistivity values in-  
41  
42 393 dicate that it is made of material coarser than the laminated clays, as shown by superficial  
43  
44 394 soil samples (sandy to gravelly clay). From a hydrogeological point of view, superficial in-  
45  
46 395 filtration tests suggest that this layer is much more permeable ( $K_s=2\times 10^{-5}$  m/s) than the  
47  
48 396 underlying clays ( $K_s\approx 1\times 10^{-6}$  m/s). This difference in permeability is supported by the  
49  
50 397 alignment of several springs and catchments at about 705 msl (Figure 8). The extension  
51  
52 398 of this shallow resistive layer is compared to the spatial zoning of sliding velocities ( $V_d$ )  
53  
54 399  
55  
56  
57  
58  
59  
60

in Figure 8. To the East, the limit between the slow motion area ( $V_d < 2 \text{ cm/yr}$ ) and the higher velocity zone ( $V_d > 3 \text{ cm/yr}$ ) is approximately located at 700 m asl, and then very well matches the resistive layer boundary. These results suggest a lithological control on the landslide activity. The upper part of the slope, which is made of a coarser and more permeable formation (labelled SC in Figure 10), is less active because of water drainage and better mechanical properties. On the contrary, the lower impermeable laminated clays, which are saturated due to water fluxes from the overlying layer, exhibit higher slide velocities. In the southern part of the slide, ERT profiles and previous investigation (Jongmans et al., 2009; Bièvre et al., 2011a) have shown that the slope is only composed of laminated clays with low resistivity ( $< 30 \Omega \cdot \text{m}$ ), even above 700 m asl. Displacement rates in this zone are the highest measured over the landslide (more than 10 cm/yr to locally 50 cm/yr). These results highlight the role of the upper geological layers on the sliding activity. For the Avignonet landslide, it turned out that the main features of the slide velocity field can be explained from spatial geological facies variations (Figure 8). More generally, these results show the importance of lithological and/or grain size variation on the movement of a landslide, as shown by laboratory flume experiments (e.g. Iverson et al., 2000; Wang and Sassa, 2003). The origin of this resistive layer is uncertain. From the geological map (Figure 1a), the upper part of the landslide is overlaid with moraine deposits at about 750 m asl. The resistive formation could then be made of creeping moraine material mixed up with laminated clays on the slope. However, the measured great thickness (over 30 m) and its southward limited extension suggest that this formation could result from a former gravitational movement, although a sedimentary origin can not be excluded. This issue has to be further investigated.

For the Avignonet landslide, the slide process understanding was initially partially



biased by the concentration of investigation in the populated areas. This study highlights the control of both vertical and horizontal lithological variations on the landslide process and the necessity of combining 3D investigation techniques for understanding the complexity of large landslide mechanism. In the future, methodologies should be developed to combine and extract information from heterogeneous data sources and to integrate it in an unbiased 3D geometrical model showing the internal layering and the slip surfaces.

## Acknowledgements

This work was partly funded by 2 IFSTTAR national programs (11R093 and 11R112), one national ANR project (SISCA) and one European program (Mountain Risks). GPS data were provided by the French observatory on landslides OMIV ([omiv.osug.fr](http://omiv.osug.fr)). The authors would like to thank Y. Orengo, R. Béthoux and L. Darras (ISTERre) for their help in the field. S. Grangeon (ISTERre Grenoble), L. Oxarango (LTHE Grenoble) and L. Lassabatère (ENTPE Lyon) are acknowledged for fruitful discussions.

## References

- Azañón, J. M., Azor, A., Yesares, J., Tsige, M., Mateos, R. M., Nieto, F., Delgado, J., López-Chicano, M., Martín, W., and Rodríguez-Fernández, J. (2010). Regional-scale high-plasticity clay-bearing formation as controlling factor on landslides in southeast Spain. *Geomorphology*, 120:26–37.
- Baldi, P., Cenni, N., Fabris, M., and Zanutta, A. (2008). Kinematics of a landslide derived from archival photogrammetry and GPS data. *Geomorphology*, 102(3–4):435–444.
- Bièvre, G., Jongmans, D., Winiarski, T., and Zumbo, V. (2011a). Application of geo-

physical measurements for assessing the role of fissures in water infiltration within a  
clay landslide (Trièves area, French Alps). *Hydrological Processes*, 25(8):n/a.

Bièvre, G., Knieß, U., Jongmans, D., Pathier, E., Schwartz, S., van Westen, C. J.,  
Villemin, T., and Zumbo, V. (2011b). Paleotopographic control of landslides in lacus-  
trine deposits (Trièves plateau, French western Alps). *Geomorphology*, 125(1):214–224.

Braud, I., De Condappa, D., Soria, J. M., Haverkamp, R., Angulo-Jaramillo, R., Galle,  
S., and Vauclin, M. (2005). Use of scaled forms of the infiltration equation for the  
estimation of unsaturated soil hydraulic properties (the Beerkan method). *European  
Journal of Soil Science*, 56(3):361–374.

Brocard, G. Y., Van Der Beek, P. A., Bourlès, D. L., Siame, L. L., and Mugnier, J.-L.  
(2003). Long-term fluvial incision rates and postglacial river relaxation time in the  
French Western Alps from 10Be dating of alluvial terraces with assessment of inheri-  
tance, soil development and wind ablation effects. *Earth and Planetary Science Letters*,  
209:197–214.

Bromhead, E. N. and Ibsen, M.-L. (2004). Bedding-controlled coastal landslides in South-  
east Britain between Axmouth and the Thames Estuary. *Landslides*, 1(2):131–141.

Coe, J. A., McKenna, J. P., Godt, J. W., and Baum, R. L. (2009). Basal-topographic  
control of stationary ponds on a continuously moving landslide. *Earth Surface Processes  
and Landforms*, 34(2):264–279.

Corsini, A., Borgatti, L., Coren, F., and Vellico, M. (2007). Use of multitemporal airborne  
LiDAR surveys to analyse postfailure behaviour of earthslides. *Canadian Journal of  
Remote Sensing*, 33(2):116–120.

- 467 Corsini, A., Pasuto, A., Soldati, M., and Zannoni, A. (2005). Field monitoring of the  
468 Corvara landslide (Dolomites, Italy) and its relevance for hazard assessment. *Geomor-*  
469 *phology*, 66(1-4):149–165.
- 470 Debelmas, J. (1967). La Chapelle-en-Vercors. In *Carte géologique de la France à 1/50000*.  
471 BRGM Éditions, Orléans, France.
- 472 Dix, C. H. (1955). Seismic velocities from surface measurements. *Geophysics*, 20:68–86.
- 473 Eilertsen, R. S., Hansen, L., Bargel, T. H., and Solberg, I.-L. (2008). Clay slides in the  
474 Målselv valley, northern Norway: Characteristics, occurrence, and triggering mecha-  
475 nisms. *Geomorphology*, 93(3-4):548–562.
- 476 François, B., Tacher, L., Bonnard, C., Laloui, L., and Triguero, V. (2007). Numerical mod-  
477 elling of the hydrogeological and geomechanical behaviour of a large slope movement:  
478 the Triesenberg landslide (Liechtenstein). *Canadian Geotechnical Journal*, 44(7):840–  
479 857.
- 480 Giraud, A., Antoine, P., Van Asch, T. W. J., and Nieuwenhuis, J. D. (1991). Geotechnical  
481 problems caused by glaciolacustrine clays in the French Alps. *Engineering Geology*,  
482 31:185–195.
- 483 Harders, R., Kutterolf, S., Hensen, C., Moerz, T., and Brueckmann, W. (2010). Tephra  
484 layers: A controlling factor on submarine translational sliding? *Geochemistry Geo-*  
485 *physics Geosystems*, 11(5):Q05S23.
- 486 Iverson, R. M., Reid, M. E., Iverson, N. R., LaHusen, R. G., Logan, M., Mann, J. E., and  
487 Brien, D. L. (2000). Acute sensitivity of landslide rates to initial soil porosity. *Science*,  
488 290:513–516.

Jongmans, D., Bièvre, G., Schwartz, S., Renalier, F., and Beaurez, N. (2009). Geophysical investigation of the large Avignonet landslide in glaciolacustrine clays in the Trièves area (French Alps). *Engineering Geology*, 109:45–56.

Lassabatère, L., Angulo-Jaramillo, R., Soria Ugalde, J. M., Cuenca, R., Braud, I., and Haverkamp, R. (2006). Beerkan Estimation of Soil Transfer Parameters through Infiltration Experiments - BEST. *Soil Science Society of America Journal*, 70(2):521–532.

Loke, M. H. and Barker, R. (1996). Rapid least-squares inversion of apparent resistivity pseudosections by a quasi-newton method. *Geophysical Prospecting*, 44:131–152.

Lorier, L. and Desvarreux, P. (2004). Glissement du Mas d'Avignonet, commune d'Avignonet. In *Proceedings of the workshop Ryskhydrogeo, Program Interreg III, La Mure (France)*, page 8 p.

Matsuoka, N., Hirakawa, K., Watanabe, T., Haeberli, W., and Keller, F. (1998). The role of diurnal, annual and millennial freeze-thaw cycles in controlling alpine slope instability. In Lewkowicz, A. G. and Allard, M., editors, *Permafrost - 7th International Conference, June 23-27, Yellowknife, Canada*, number 55 in Nordicana, pages 711–717.

Monjuvent, G. (1973). La transfluence Durance-Isère. Essai de synthèse du Quaternaire du bassin du Drac (Alpes françaises). *Géologie Alpine*, 49:57–118.

Oldenburg, D. W. and Li, Y. (1999). Estimating depth of investigation in DC resistivity and IP surveys. *Geophysics*, 64(2):403–416.

Petley, D. N., Mantovani, F., Bulmer, M. H., and Zannoni, A. (2005). The use of surface monitoring data for the interpretation of landslide movement patterns. *Geomorphology*, 66(1-4):133–147.

- 511 Picarelli, L. (2000). Mechanisms and rates of slope movements in fine grained soils. In  
512 *Int. Conf. Geotech. Geol. Eng. Geoeng.*, volume 1, pages 1618–1670.
- 513 Picarelli, L., Urciuoli, G., and Russo, C. (2004). The role of groundwater regime on  
514 behaviour of clayey slopes. *Canadian Geotechnical Journal*, 41:467–484.
- 515 Renalier, F., Bièvre, G., Jongmans, D., Campillo, M., and Bard, P.-Y. (2010a). Charac-  
516 terization and monitoring of unstable clay slopes using active and passive shear wave  
517 velocity measurements. In Miller, R. D., Bradford, J. D., and Holliger, K., editors,  
518 *Advances in near-surface seismology and ground-penetrating radar*, number 15 in Geo-  
519 physical Developments Series, pages 397–414. Society of Exploration Geophysics, Tulsa,  
520 USA.
- 521 Renalier, F., Jongmans, D., Campillo, M., and Bard, P.-Y. (2010b). Shear wave veloc-  
522 ity imaging of the Avignonet landslide (France) using ambient noise cross-correlation.  
523 *Journal of Geophysical Research*, 115:F03032.
- 524 Requillard, J.-P. and Moulin, C. (2004). Glissement du mas sur la commune d'Avignonet  
525 (France). État de la gestion du risque en octobre 2004. In *Proceedings of the workshop*  
526 *Ryskhhydrogeo, Program Interreg III, La Mure (France)*, page 22.
- 527 Rott, H., Scheuchl, B., Siegel, A., and Grasemann, B. (1999). Monitoring very slow slope  
528 motion by means of SAR interferometry: A case study from a mass waste above a  
529 reservoir in the Ötztal Alps, Austria. *Geophysical Research Letters*, 26(11):1629–1632.
- 530 Sandmeier, K. J. (2010). *Reflexw 5.5 user guide*. Sandmeier Scientific Softwares  
531 (www.sandmeier-geo.de), Karlsruhe, Germany.
- 532 Serra, O. (2008). *The well logging handbook*. Éditions Technip, Paris, France.

533 Squarzoni, C., Delacourt, C., and Allemand, P. (2003). Nine years of spatial and temporal  
534 evolution of the La Valette landslide observed by SAR interferometry. *Engineering*  
535 *Geology*, 68:53–66.

536 Stiros, S. C., Vichas, C., and Skourtis, C. (2004). Landslide monitoring based on geodet-  
537 ically derived distance changes. *Journal of Surveying Engineering*, 130(4):156–162.

538 Strozzi, T., Farina, P., Corsini, A., Ambrosi, C., Thüning, M., Zilger, J., A., W.,  
539 Wegmüller, U., and Werner, C. (2005). Survey and monitoring of landslide displace-  
540 ments by means of L-band satellite SAR interferometry. *Landslides*, 2:193–201.

541 Telford, W. M., Geldart, L. P., and Sheriff, R. E. (1990). *Applied geophysics*. Cambridge  
542 University Press, Cambridge, 2nd edition.

543 Teza, G., Pesci, A., Genevois, R., and A., G. (2008). Characterization of landslide ground  
544 surface kinematics from terrestrial laser scanning and strain field computation. *Geo-*  
545 *morphology*, 97(3-4):424–437.

546 Travelletti, J. and Malet, J.-P. (2011). Characterization of the 3D geometry of flow-like  
547 landslides: A methodology based on the integration of heterogeneous multi-source data.  
548 *Engineering Geology*, in press.

549 Travelletti, J., Malet, J.-P., Samyn, K., Grandjean, G., and Jaboyedoff, M. (2011). Control  
550 of landslide retrogression by discontinuities: evidences by the integration of airborne-  
551 and ground-based geophysical information. *Landslides*, in press.

552 Van Asch, T. W. J., Malet, J.-P., and Van Beek, L. (2006). Influence of landslide geometry  
553 and kinematic deformation to describe the liquefaction of landslides: Some theoretical  
554 considerations. *Engineering Geology*, 88(1-2):59–69.

555 Wang, G. and Sassa, K. (2003). Pore-pressure generation and movement of rainfall-  
556 induced landslides: effects of grain size and fine-particle content. *Engineering Geology*,  
557 69:109–125.

558 Wentworth, C. K. (1922). A scale of grade and class terms for clastic sediments. *Journal*  
559 *of Geology*, 30(5):377–392.

560 Yilmaz, D., Lassabatère, L., Angulo-Jaramillo, R., Deneele, D., and Legret, M. (2010).  
561 Hydrodynamic characterization of basic oxygen furnace slag through an adapted BEST  
562 method. *Vadose Zone Journal*, 9(1):107–116.

Table 1: Borehole logs and depth of slip surfaces, from [Requillard and Moulin \(2004\)](#), [Jongmans et al. \(2009\)](#) and [Bièvre et al. \(2011a\)](#). T0 to T3: drillings; T4: coring.

Borehole	Elevation of the borehole head (m asl)	Geological formations	Depth of slip surfaces
T0	716	0-5 m: morainic colluvium	5 m
		5 - 83 m: laminated clays	10 m
		83-89: silts and pebbles	47 m
T1	676	0-5 m: morainic colluvium	15 m
		5 – 56.5 m: laminated clays	34 m
		56.5 – 59 m: alluvial deposits	42.5 m
T2	651	0-4 m: morainic colluvium	1.5 m
		4 – 14.5 m: laminated clays	4 m
		14.5 – 17 m : alluvial deposits	12 m
T3	663	0-4.7 m: morainic colluvium	17 m
		4.7 – 20.5 m: laminated clays	
T4	692.5	0-2.5 m: morainic colluvium	5 m
		2.5-18.5 m: blocky clays	10 to 15 m
		18.5 – 49.5 m: laminated clays	42 m



Table 2: ERT profiles acquisition and inversion parameters.

Profile	Number of electrodes	Electrode spacing (m)	Profile length (m)	Measurements	Iterations	Absolute error (%)
E1	64	5	315	651	3	2.2
E2	64	5	315	647	3	2.4
E3	48	5	235	358	3	3
E4	48	5	235	359	3	1.4
E5	48	5	235	360	3	2.4
E6	32	4	124	153	3	2.1
E7	48	5	235	360	3	1.4
E8	80	5	395	884	3	1.98
E9	48	5	235	315	2	1.7
E10	64	5	315	540	3	4.9

Table 3: Geotechnical and hydraulic properties measured at the 5 infiltration sites. Grain size distribution is expressed as weight percentage of soil type, according to the Wentworth scale (Wentworth, 1922). Saturated hydraulic conductivities (Ks) are obtained by BEST analysis, and steady-state infiltration rates (SIR) are derived from Beerkan infiltration experiments (Figure 9). FM: fissure and soil matrix. X: BEST analysis not possible.

Test	Granulometry (%)			Bulk density (g/cm3)	Dry bulk density (g/cm3)	Volumetric water content (%)	Porosity (%)	Permeability Type	SIR (m/s)	Ks (m/s)
	Silt/Clay	Sand	Gravel							
I1	47.3	27.3	25.4	1.49	1.09	18.24	58.9	Matrix	1x10 <sup>-4</sup>	2.1x10 <sup>-5</sup>
I2	64.5	20.3	15.2	1.84	1.565	27.5	40.8	Matrix	3x10 <sup>-6</sup>	8.1x10 <sup>-7</sup>
I3	66.5	18.4	15.1	1.67	1.44	23.23	45.7	Matrix	1x10 <sup>-5</sup>	2x10 <sup>-6</sup>
I4	65.8	20.6	13.6	1.44	0.92	16.47	65.3	Fissures	4x10 <sup>-5</sup>	X
								FM	4x10 <sup>-6</sup>	X
I5	91.2	4.6	4.6	2.09	1.39	31.67	47.5	Fissures	4x10 <sup>-5</sup>	X
								FM	1x10 <sup>-5</sup>	X

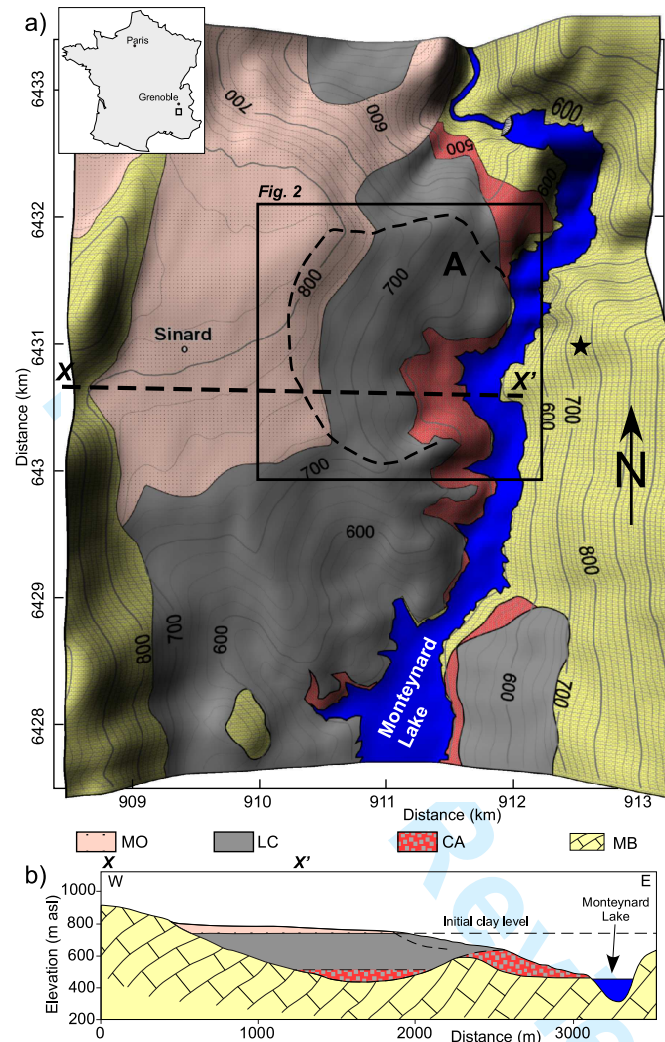


Figure 1: Location and geology of the study site. a) Geological map, adapted from Debelmas (1967) and Monjuvent (1973) with the Avignonet landslide extension and the location of the geological cross-section XX' shown in Figure 1b. Coordinates are kilometric and expressed in the Lambert-93 French system. Black star indicates the position from where picture in Figure 3a was shot. MO: Moraines; LC: Laminated Clays; CA: Compact and locally cemented Alluvium; MB: Mesozoic Bedrock. b) Geological cross-section XX'.

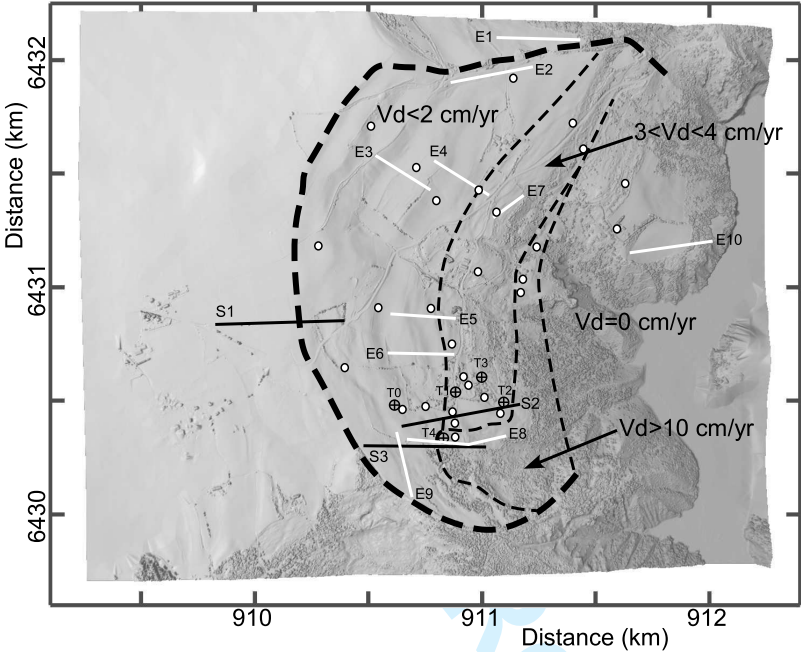


Figure 2: Morphology of the study area (obtained from a LiDAR scan acquisition in 2006) with the contour of the Avignonet landslide (thick dashed line), the position of 28 geodetic stations (white dots), the limits between the slide velocity zones (thin dashed lines), and the location of the drillings (T0 to T4) and of the geophysical profiles (black lines: seismic profiles S1 to S3; white lines: electrical profiles E1 to E10).

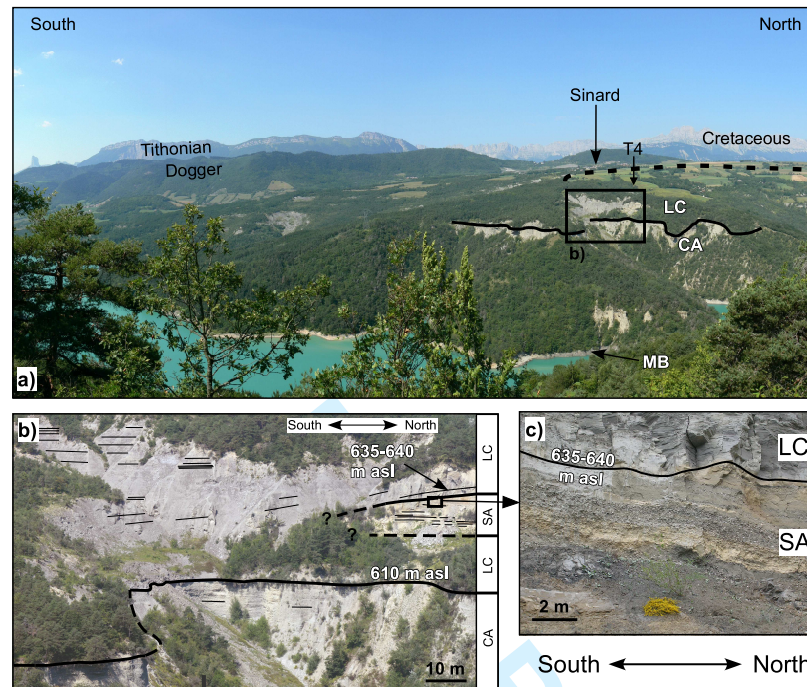


Figure 3: Outcrop pictures. a) General view of the Avignonet landslide from the Drac opposite bank. Picture was taken from the location indicated by a black star in Figure 1. Location of drilling T4 is indicated. LC: laminated clays; CA: compact and locally cemented alluvium; MB: Mesozoic Bedrock. The continuous black line corresponds to the interface between CA and LC. Black dashed line stands for the Avignonet landslide limit. b) Detail of the transition between CA and the overlying clays LC, with the interbedded 10 to 15 m thick soft alluvium layer (SA). c) Detail of the upper limit of the SA layer.

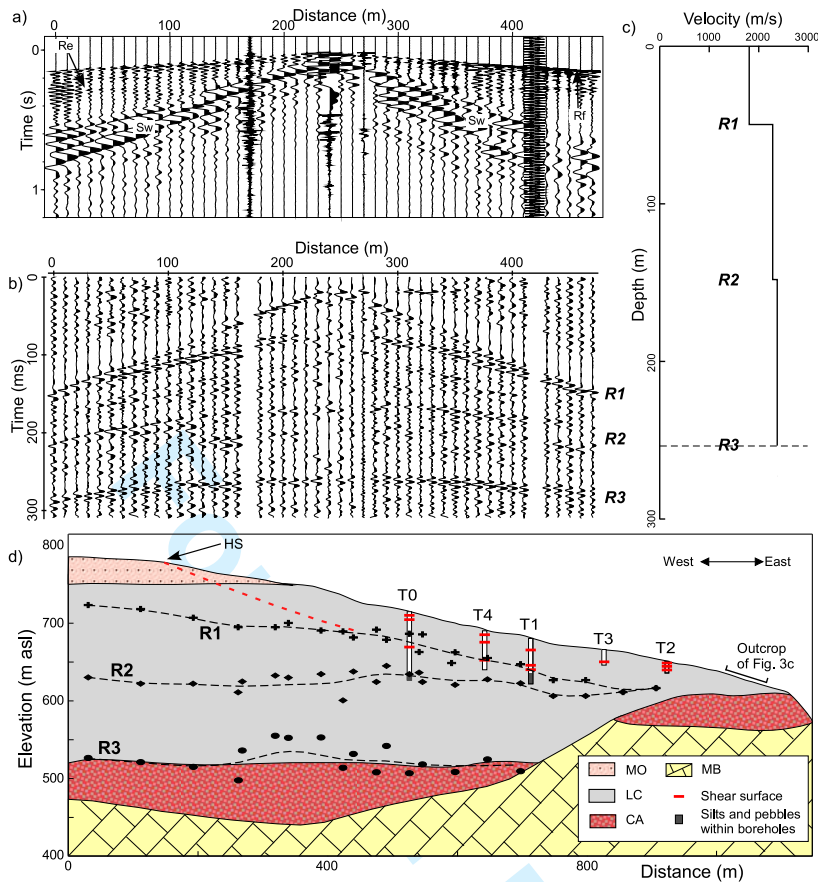


Figure 4: Reflections along seismic profiles. a) Raw seismogram for a shot at 240 m along profile S1. Rf: refracted waves; Re: reflected waves; Sw: Surface waves. b) Same profile, with bandpass filtering and AGC correction. Three main reflections (R1 to R3) are observed. c) 1D depth-velocity model from reflection analysis. d) Geological cross-section across Avignonet landslide with reflectors R1 to R3 (crosses, diamonds, ellipses and mean depth curves in black dashed lines). Drillings T0 to T4 are indicated with the position of slip surfaces (horizontal red lines) and silts and pebbles (grey fill). The red dashed line stands for the position of the deep slip surface. HS : landslide headscarp; MO: Moraines; LC: Laminated Clays; CA: Compact and locally cemented Alluvium; MB: Mesozoic Bedrock. The position of sands and pebbles observed at outcrop (Figure 3c) is indicated.



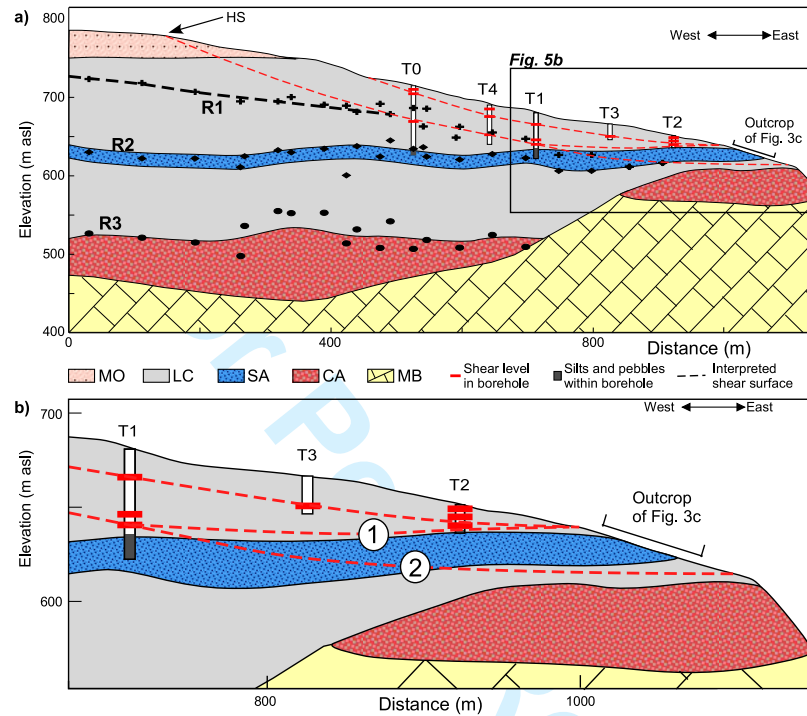


Figure 5: Geological and geotechnical model deduced from the analysis of P-wave reflections R1 to R3. MO: Moraines; LC: Laminated Clays; SA: Soft Alluvium; CA: Compact and locally cemented Alluvium; MB: Mesozoic Bedrock. a) General model over the Avignonet landslide (same cross-section as in Figure 4d) with the possible location and lateral continuity of slip surfaces (red dashed lines). b) Close-up of the toe of the landslide with two possible interpretations (labelled 1 and 2) for the daylight of the deep slip surface.

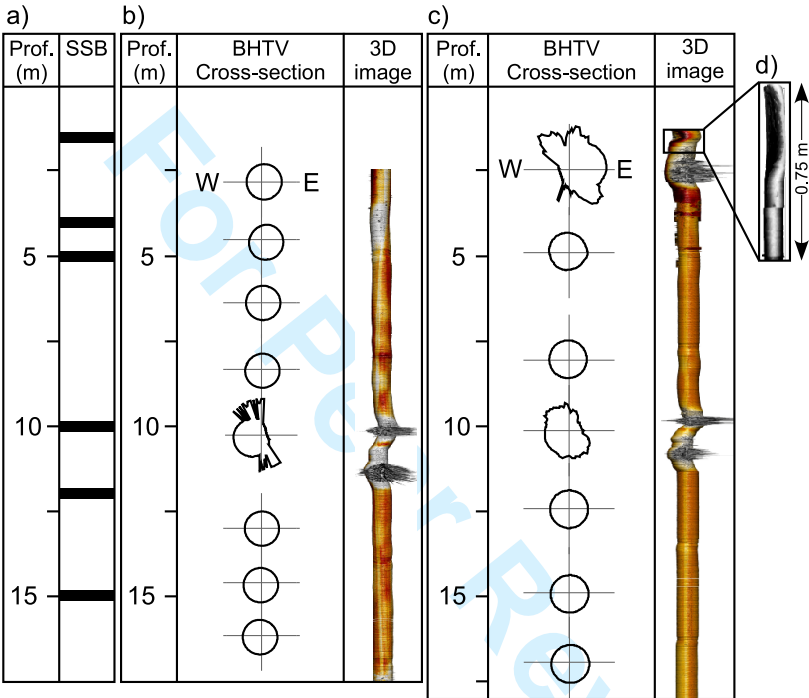


Figure 6: Acoustic imaging within boreholes T4a and T4b located 8 m West and 9 m East of T4, respectively. a) Slip surfaces detected in boreholes (SSB) T0 to T4 (details in Table 1). b) and c) BHTV cross-section and 3D image in T4a and T4b, respectively. d) BHTV 3D image zoom of the shallowest deformation in T4b.



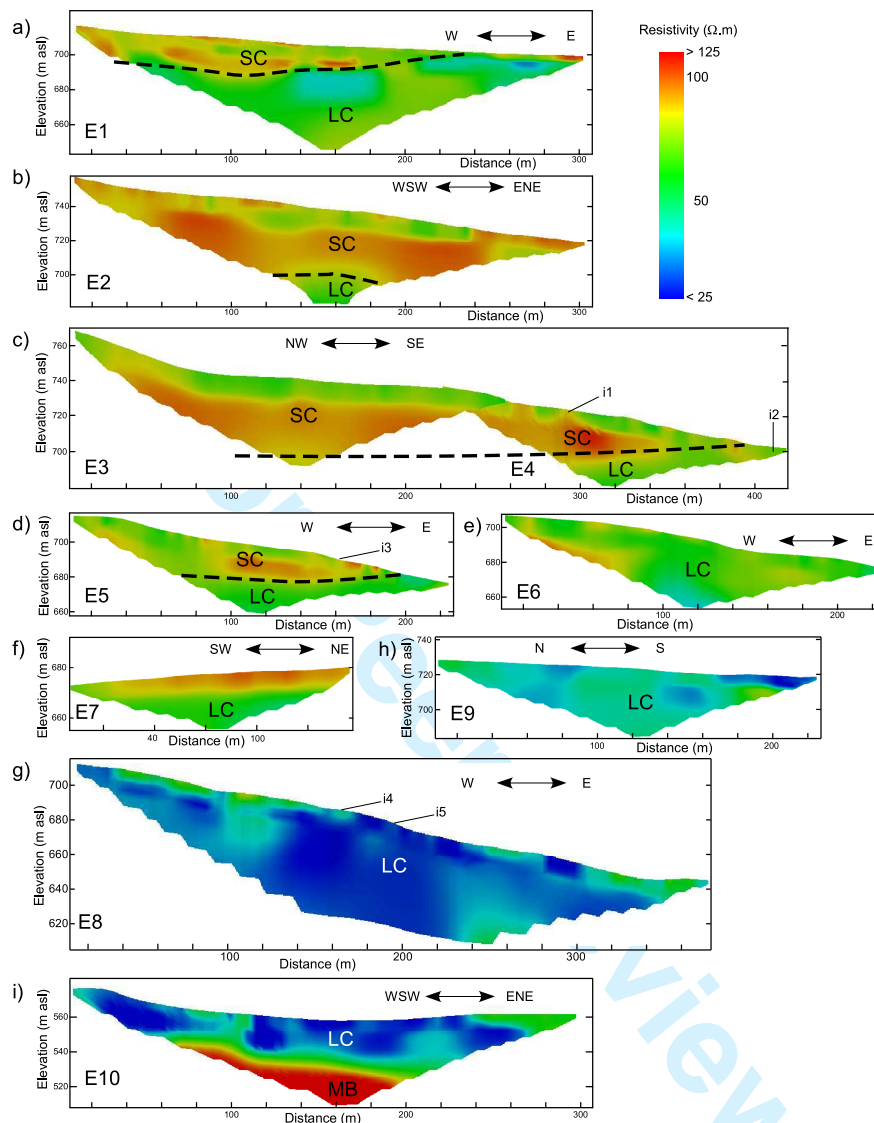


Figure 7: ERT profiles (location in Figure 2). Absolute errors are lower than 5% after a maximum of 3 iterations (details are provided in Table 2). Location of Beerkan tests i1 to i5 is indicated. a) Profile E1. b) Profile E2. c) Profiles E3 and E4. d) Profile E5. e) Profile E6. f) Profile E7. g) Profile E8. h) Profile E9. i) Profile E10. SC: sandy to blocky clays; LC: laminated clays; MB: Mesozoic bedrock.

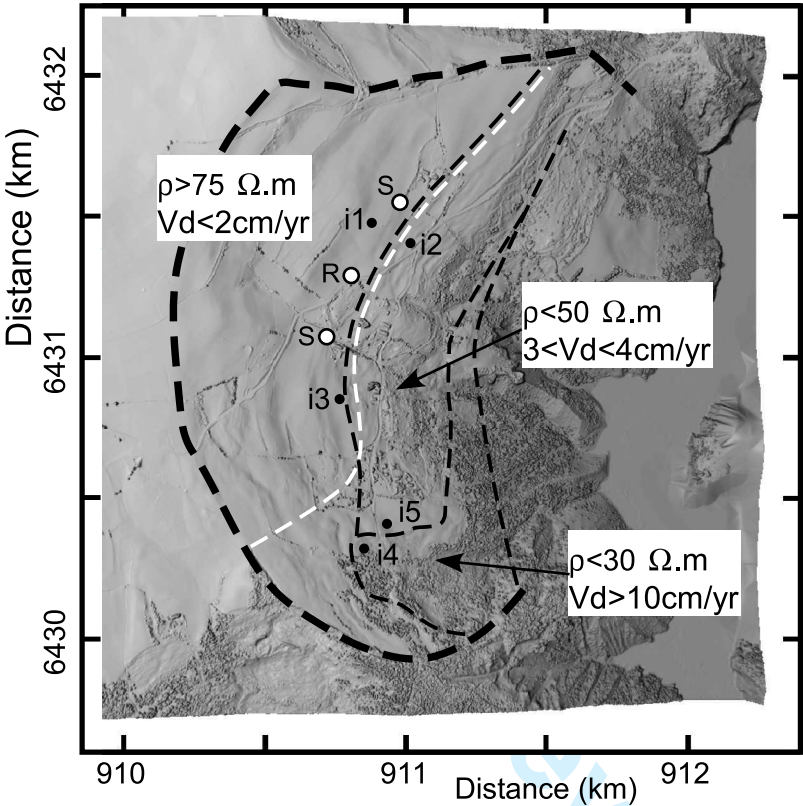


Figure 8: Spatial extent of the limit (white dashed line) between the resistive ( $> 75 \Omega.m$ ), intermediate ( $< 50 \Omega.m$ ) and conductive ( $< 30 \Omega.m$ ) layers over the Avignonet landslide. The zoning in slide velocities (three classes) is indicated with black dashed lines. The location of two water catchments (S), of one seeping resurgence (R) and of the hydrological tests i1 to i5 is shown. AA': cross-section of Figure 10.

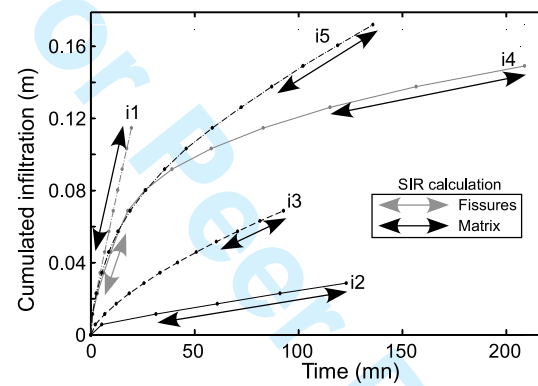


Figure 9: Infiltration curves for tests i1 to i5 (see location in Figure 8). Steady state infiltration rates (SIR given in Table 3) were deduced for the curve parts shown with double-arrowed lines.

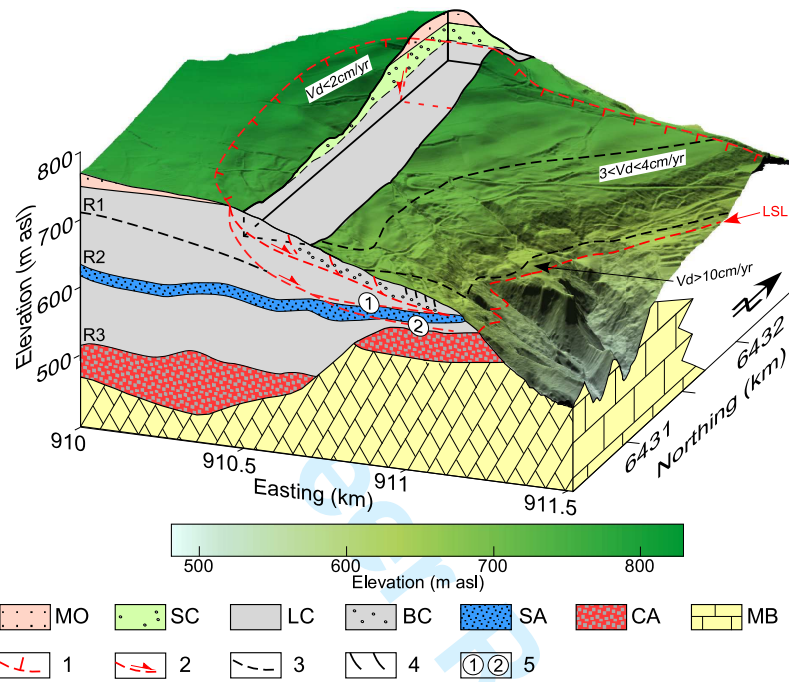


Figure 10: Synthetic interpretative 3D geological and geotechnical model. MO: Moraines; SC: Sandy Clays; LC: Laminated Clays; BC: Blocky Clays; SA: Soft Alluvium; CA: Compact and locally cemented Alluvium; MB: Mesozoic Berock. LSL : Landslide lower limit. 1: Landslide limit at surface; 2: Slip surface; 3: Velocity zone; 4: Fissured clays at the toe of the slide; 5: Two possible interpretations for the daylight of the deep slip surface (see Figure 5).